Applied Surface Science 399 (2017) 480–490

Contents lists available at ScienceDirect

Applied Surface Science

journal homepage: www.elsevier.com/locate/apsusc

Full Length Article

Nanosecond laser texturing of uniformly and non-uniformly wettable micro structured metal surfaces for enhanced boiling heat transfer

Matevž Zupančič*, Matic Može, Peter Gregorčič, Iztok Golobič

Faculty of Mechanical Engineering, University of Ljubljana, Aškerčeva 6, 1000 Ljubljana, Slovenia

ARTICLE INFO

Article history:
Received 22 September 2016
Received in revised form
11 December 2016
Accepted 15 December 2016
Available online 15 December 2016

Keywords:
Nanosecond laser
Surface texturing
Non-uniform wettability
Microcavities
Nucleation criteria
Enhanced boiling heat transfer

ABSTRACT

Microstructured uniformly and non-uniformly wettable surfaces were created on 25-μm-thin stainless steel foils by laser texturing using a marking nanosecond Nd:YAG laser (λ = 1064 nm) and utilizing various laser fluences and scan line separations. High-speed photography and high-speed IR thermography were used to investigate nucleate boiling heat transfer on the microstructured surfaces. The most pronounced results were obtained on a surface with non-uniform microstructure and non-uniform wettability. The obtained results show up to a 110% higher heat transfer coefficients and 20–40 times higher nucleation site densities compared to the untextured surface. We show that the number of active nucleation sites is significantly increased in the vicinity of microcavities that appeared in areas with the smallest (10 μm) scan line separation. Furthermore, this confirms the predictions of nucleation criteria and proves that straightforward, cost-effective nanosecond laser texturing allows the production of cavities with diameters of up to a few micrometers and surfaces with non-uniform wettability. Additionally, this opens up important possibilities for a more deterministic control over the complex boiling process.

1. Introduction

Nucleate boiling is a phase change heat transfer mechanism and is one of the most effective and technically controllable approaches for removal of high heat flux. Its performance is usually quantified by two characteristic parameters, heat transfer coefficient and critical heat flux (CHF). The first one is defined as the ratio between heat flux transmitted from the surface, and the wall superheat, while the latter represents the upper limit of the nucleate boiling regime. The desire to increase both the heat transfer coefficient and the CHF has led to the development of various surface modification techniques in the last decades as the surface and its interaction with the working fluid have a profound effect on the boiling phenomenon. Studies on hydrophobic (water-repellent) and hydrophilic (water-loving) surfaces have already shown some key improvements [1–8].

Hydrophobic surfaces prefer to be in contact with the vapor phase rather than the liquid water and therefore promote the activation of nucleation [1]. At the same time, they provide larger bubble departure diameters and the bubbles are more likely to coalesce. Reduction of wettability reduces the temperature of the onset of nucleate boiling [2] and increases the heat transfer coefficient at low heat fluxes. As the heat flux increases, the formation of large vapor blankets [3] decreases heat transfer and promotes the CHF conditions. On the contrary, hydrophilic surfaces increase the "suction" of the liquid towards the nucleation sites, decrease bubble contact diameters [3,4], and, finally, delay the CHF due to the water replenishment on dry spots. However, because of the increased wettability, hydrophilic surfaces require larger superheat for nucleate boiling to occur and do not necessarily provide an enhanced heat transfer coefficient at low heat fluxes [3]. For further enhancements, several authors already suggested simultaneous implementation of hydrophobic and hydrophilic features on a single surface to produce a so called biphilic surface [3,6,7,9].

Another approach of boiling enhancement is incorporation of pores or micro cavities onto the surface [10,11]. According to the existing nucleation criteria [12,13], a conically-shaped cavity on the surface might serve as an active nucleation site if the diameter of this cavity falls within a certain range. This size range depends on the wall superheat and contact angle. To provide large number of potentially active nucleation sites at different wall superheats, the surface should incorporate various contact angles (e.g. non-uniform wettability [14]) as well as wide range of cavity diameters [15]. A recent study of flow boiling in microchannels [15] proved that porous multi-scale rough surface significantly enhances bubble nucleation and considerably mitigates two-phase flow instabilities.

* Corresponding author.
E-mail address: matevz.zupancic@fs.uni-lj.si (M. Zupančič).

http://dx.doi.org/10.1016/j.apsusc.2016.12.120
0169-4332/

Mechanical resistance, thermal stability and challenging production [16] are still the main drawbacks preventing wider implementation of hydrophilic and hydrophobic surfaces in heat transfer applications. In our previous study [3], we demonstrated boiling heat transfer enhancement on biphilic surfaces comprised of polydimethylsiloxane-silica films. The transition of wettability from hydrophobic to hydrophilic was achieved by locally heating the coating using a pulsed Nd:YAG laser. However, the coatings in general have significant drawbacks for real applications. Modifying surfaces' wettability and micro/nanostructure by laser texturing of non-coated surfaces is a relatively simple, fast, and highly flexible approach. It is also more environmentally acceptable and there are no problems with adhering any coating to the surface. In pool boiling, recent study by Kruse et al. [5] on superhydrophilic stainless steel surfaces, processed by femtosecond laser pulses, showed both a considerable increase of the CHF from 910 kW/m^2 to 1420 kW/m^2 as well as a significant increase of the heat transfer coefficient from 23 kW/m^{2}K to 68 kW/m^{2}K. However, most of the reported work on laser micro/nanostructuring relies on costly ultrafast lasers [5,17,18].

The main objective of this study is to incorporate advantages of wettability modifications together with microstructure and micro cavities to develop surfaces for enhanced nucleate boiling heat transfer. Additional aim is to achieve this by using a nanosecond marking laser, which represents a cost-effective alternative to currently utilized laser-processing technologies for surface wettability and microstructure modifications. Surfaces were developed on stainless steel, which was used due to its widespread applications in heat and process engineering, good resistance to corrosion, and because the results of previous research indicate the possibility of modifying its wettability using nanosecond laser pulses [19]. In order to study the durability of the textured surfaces in a boiling heat transfer application, we performed several consecutive saturated pool boiling experiments. We employed high-speed IR thermography and high-speed recordings to obtain a visualization of the departing bubbles with the corresponding local wall temperature measurements. Surfaces were characterized before and after boiling experiments through contact angle measurements. Our experiments show that surfaces produced by nanosecond laser texturing have the potential to be a good alternative to those modified using currently established techniques.

2. Nucleation criteria

The impact of surface material, texture and topography on nucleate boiling phenomenon has long been investigated [20]. Influences on bubble growth were first researched by Bankoff [21], Griffith and Wallis [22], and Han and Griffith [23]. One of the first nucleation criteria for dimensioning of potential active nucleation sites was developed by Hsu [12]. Hsu's model considers a bubble nucleus sitting at the mouth of a cavity with the radius r_c surrounded by the liquid in the saturated state. At the beginning of a bubble growth cycle, only the surface is uniformly superheated to ΔT above the saturation temperature (T_{sat}). Gradually, the liquid is warmed through transient-conduction process, which in turn causes the thermal layer to grow. This growth is limited by a strong turbulence in the liquid. Beyond a certain thickness, the temperature of the liquid is considered to be constant at bulk temperature (T_{bulk}). The model predicts that the bubble will start to grow if fluids' temperature within the thermal layer reaches the saturation temperature inside the bubble. By combining the Clausius-Clapeyron equation for saturated temperature, Gaussian expression for surface tension, Carslaw and Jaeger model for the temperature profile inside the thermal layer [24] and geometrical relations, a quadratic equation can be obtained. Its solutions [Eq. (1)] represent the upper

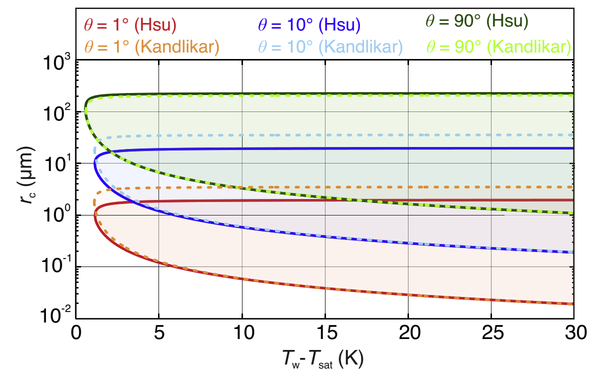

Fig. 1. Effective nucleation cavity radius versus wall temperature for surfaces with different wettabilities. The example considers saturated boiling of pure water at atmospheric pressure (σ = 72 mN/m).

($r_{c,max}$) and the lower ($r_{c,min}$) limit of the potential active nucleation cavities radii at a given superheat by taking into account the thermal properties of the liquid and its interaction with the surface through contact angle θ:

$$\left\{r_{c,\min}, r_{c,\max}\right\} = \frac{\delta}{2}\left(\frac{\sin\left(\theta\right)}{1+\cos\left(\theta\right)}\right)\left(1 \mp \sqrt{1-\frac{8\sigma_{LV}T_{sat}\left(1+\cos\left(\theta\right)\right)}{h_{LV}\rho_V\left(T_w-T_{sat}\right)\delta}}\right) \quad (1)$$

Eq. (1) accounts for the surface tension between the liquid and the vaporous phase (σ_{LV}), saturation temperature (T_{sat}), wall temperature (T_w), latent heat of vaporization (h_{LV}), and the density of the vapor (ρ_V). Thermal layer thickness (δ) is calculated by dividing the thermal conductivity of the working fluid (λ) with its heat transfer coefficient (α) for natural convection. If the discriminant of the quadratic equation is negative, nucleate boiling is not taking place on the surface. As the thickness of the thermal layer constantly changes due to turbulence, the solutions of the quadratic equation are subject to perpetual change as well.

Kandlikar et al. [13,25] numerically simulated liquid flow around a growing bubble and derived a nucleation criterion by comparing the equilibrium pressure corresponding to the radius of the forming bubble with the liquid temperature at the location of the streamline passing over the top of the forming bubble. The final equations for the minimum and maximum radii of the potential active nucleation sites are remarkably similar to those originating from Hsu's model but are able to account for the potential subcooled state of the liquid and use the receding contact angle θ_r instead of equilibrium contact angle used in Hsu's model:

$$\left\{r_{c,\min}, r_{c,\max}\right\} = \frac{\delta\sin\left(\theta_r\right)}{2.2}\left(\frac{T_w-T_{sat}}{T_w-T_{bulk}}\right)\left(1 \mp \sqrt{1-\frac{8.8\sigma_{LV}T_{sat}\left(T_w-T_{bulk}\right)}{h_{LV}\rho_V\left(T_w-T_{sat}\right)^2\delta}}\right) \quad (2)$$

Possible application of both aforementioned nucleation criteria is shown in Fig. 1, where the theoretical results for different surface wettabilities are shown with different colors. Saturated boiling of pure water with a thermal conductivity of 0.679 W/mK and a heat transfer coefficient of 3000 W/m^{2}K is considered; multiple wettabilities of the heating surface are contemplated. At a higher superheat, the size range of potential active nucleation sites is greater and the desired cavity radii are smaller on surfaces with higher wettability, i.e. lower contact angles. The differences between the criteria are small for highly wettable surfaces and almost negligible for surfaces with a contact angle close to 90°.

The following conclusions can be derived from the presented (Fig. 1) nucleation criteria. First and foremost, non-uniform wettability of the surface is desirable since it means that the radii of the potential active nucleation sites can be located anywhere in

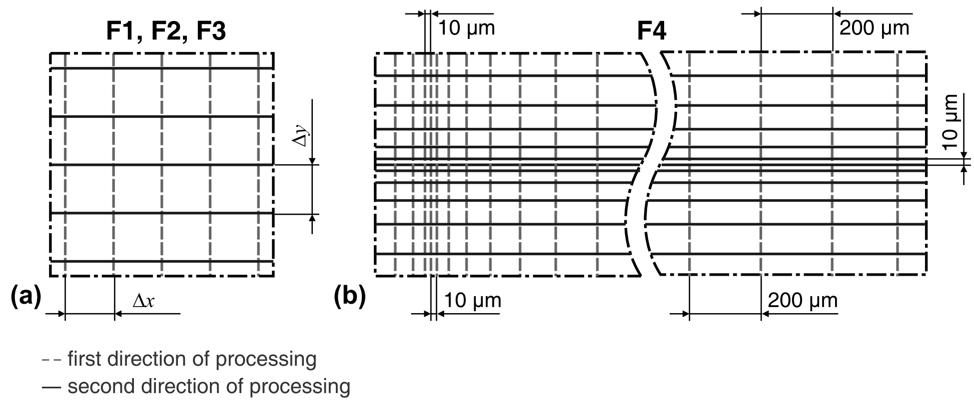

Fig. 2. Scan lines separations used in laser surface texturing.

the size range spanning across at least two to four orders of magnitude. Furthermore, nucleate boiling will first occur at a slightly lower superheat on surfaces with a lower wettability. Hence, it is feasible for such areas to be present on the surface despite their disadvantages in regard to the ability of achieving high critical heat fluxes.

To summarize, both non-uniform wettability of the surface and multi-scale cavity radii [15] are desirable in an effort to improve nucleate boiling heat transfer by surface modification. This is the reason behind our decision to also perform experiments on a surface with non-uniform wettability.

3. Experiments and methods

3.1. Laser texturing

Surfaces were textured using a marking nanosecond pulsed laser Nd:YAG (LPKF, OK DP10) with a wavelength of 1064 nm. The laser system was equipped with a scanning head (Scanlab SCANgine 14) and an F-Theta focusing lens allowing the delivery of a focused laser beam over the sample surface with beam spot diameter of 0.03 mm (defined as $1/e^2$ of the peak intensity). As samples we used 25-μm-thick AISI 316 (EN 1.4401, ISO X5CrNiMo17-12-2) stainless steel foils (Precision Brand).

Laser pulse duration of 40 ns and repetition rate of 25 kHz were used for all texturing processes. Microstructuring on the foils' surfaces was performed by scanning the surface with the laser beam using a constant speed of 150 mm/s, first in the y and then in the x direction (e.g., see Fig. 2). Four different sets of parameters were used to create surfaces F1–F4 with different micro and nanostructures. Here, we varied *(i)* the average laser power resulting in different fluencies, and *(ii)* the distance between adjacent laser scanning lines – the so-called scan line separation.

The parameters for laser texturing of surfaces F1–F4 are shown in Table 1. For surfaces F1–F3, the scan line separation in horizontal (Δx) and vertical (Δy) direction was kept constant; it was $\Delta x = \Delta y = 50\,\mu$m for surface F1, and $\Delta x = \Delta y = 10\,\mu$m for surfaces F2 and F3 [e.g., see Fig. 2(a)]. Contrarily, surface F4 was processed by a variable scan line separation. The latter changed periodically from 10 μm to 200 μm and then back to 10 μm by a step of 10 μm, i.e., $\Delta x = \Delta y = \{10, 20, \ldots, 200, \ldots 20, 10\}$ μm as it is schematically shown in Fig. 2(b). Variable scan line separation on surface F4 resulted in a heterogeneous surface texture shown in a microscope image in Fig. 3.

The surfaces were cleaned before laser processing by being wiped clean using 2-propanol (≥99,8%, Riedel-da Haën) and after processing by being dipped into 2-propanol for one minute.

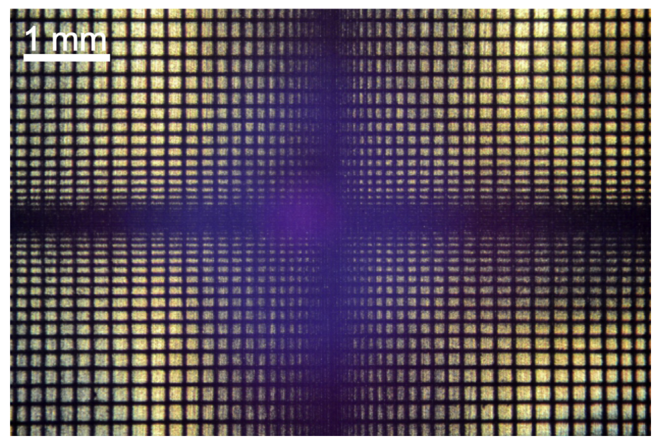

Fig. 3. Microscope image of non-uniformly textured surface F4.

3.2. Pool boiling setup

The experimental setup for pool boiling experiments on thin conductive foils allows for the measurement of characteristic boiling heat transfer parameters, visualization of the boiling process in visible spectrum, and observation of unsteady temperature fields on the surface via high-speed IR thermography. A detailed description of the experimental setup can be found elsewhere [3]; therefore, here we only briefly summarize its crucial components.

The setup is shown in Fig. 4. It consists of a boiling chamber with external dimensions of $170 \times 100 \times 100\,\text{mm}^3$, comprised of two steel plates and double glazed vertical glass walls which enable observation of the bubble growth and departure. The heater unit consisting of a ceramic base and stainless steel foil with the effective heat transfer area of $17 \times 27\,\text{mm}^2$ mounted onto nickel plated copper electrical contacts (e.g., see the bottom right side of Fig. 4) was inserted into the chamber. The bottom side of the foil was covered with high emissivity paint and the ceramic base had a rectangular hole milled into it, both of which allowed for the use of a high-speed IR camera for temperature measurements and temperature field visualization. A golden mirror at a 45° angle was used to avoid positioning the IR camera directly below the chamber.

Double-distilled water was used as the working fluid in all experiments and was vigorously boiled before each series of measurements in order to remove most of the dissolved gases. An immersed cartridge heater was utilized for preheating and to maintain the saturated state of the water during consecutive measurements. During each measurement in a series, the cartridge heater was turned off for few seconds to prevent it from influ-

Table 1
Parameters of laser texturing.

Sample	Parameter		
	Scan line separation (see Fig. 2) Δx (μm) × Δy (μm)	Pulse energy (μJ)	Pulse fluence ($\mathrm{J\,cm^{-2}}$)
F1	50 × 50	32	4.0
F2	10 × 10	32	4.0
F3	10 × 10	48	6.0
F4	variable, (10–200) × (10–200)	72	9.0

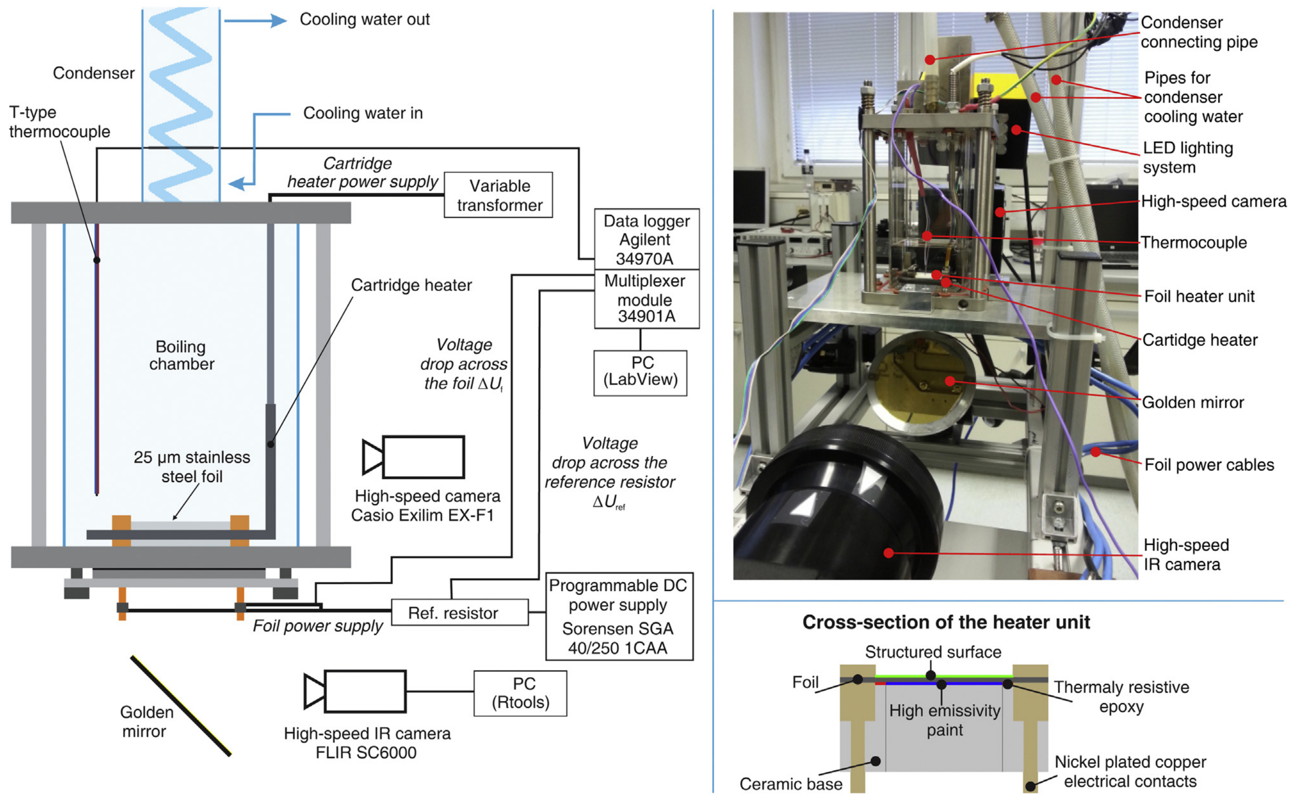

Fig. 4. Schematics (left) and photography (right) of the experimental setup for pool boiling experiments. A cross-section view of the thin metal foil heater unit is shown in the bottom right.

encing movements of the water in the boiling chamber. A T-type thermocouple was used to measure the temperature of the water (measurement accuracy for class 1 thermocouple is 1.0 K). Vaporized water was condensed using a custom-made glass condenser and a separate water cooling circuit. The foil was heated using the principle of Joule heat generation due to electrical resistance of the foil when supplied with electrical current through Sorensen SGA 40/250 DC power supply. Heat flux was calculated from the voltage drop across the foil and the DC current which was determined through the voltage drop on a reference resistor. To obtain the heat flux, the heat generation was divided by the effective heat transfer surface area of the foil; uniform heat generation was assumed across the entire foil surface. The heat fluxes used for testing of the surfaces ranged from 0 to 300 $\mathrm{kW/m^2}$ or 0–400 $\mathrm{kW/m^2}$. Thermocouple temperature and voltage drop signals were recorded using an Agilent 34970A data acquisition unit.

The boiling process was visualized in visible spectrum (for analysis of bubbles formation and their dynamics) by using a high-speed camera Casio Exilim EX-F1 (recording at 1200 fps).

3.2.1. Measurement uncertainty

A high-speed IR camera FLIR SC6000 with a cooled detector was used for temperature field visualization and wall-temperature measurements. Contactless measurements, high achievable recording speeds and high sensitivities are one of the major advantages of IR cameras. Therefore, they were successfully utilized in many pool boiling and flow boiling studies [26–29]. In our case average wall temperature was calculated from a 10 s recording of the high-speed IR camera by spatial and temporal averaging of the two-dimensional temperature fields. Recording speed was set to 1000 fps, while spatial resolution was 250 μm per pixel. Raw digitalized IR camera signal was converted to temperatures via the calibration curve obtained under the same ambient conditions that were present during the actual experiments. The expanded absolute measurement uncertainty of the temperature was determined to be 2.0 K and was practically constant across the entire calibration range of 80–180 °C. We must emphasize that our camera provides a noise equivalent differential temperature (NEDT) of only 20 mK. The measurement uncertainty of the temperature difference between individual pixels is therefore much lower than absolute temperature uncertainty.

The expanded relative measurement uncertainty of the heat flux was estimated to be 0.5% and results from the combined uncertainty of voltage drop across the foil measurements, heater area uncertainty, and electrical current measurement uncertainty. The uncertainty of the heat transfer coefficient is influenced by both the

Table 2
Equipment used for surface analyses.

Analysis	Equipment
SEM	Scanning electron microscope JEOL JSM-IT100 (magnification 5–300,000×)
Optical interferometry	3D optical microscope Bruker ContourGT-K0 (white and green light interferometry, lateral resolution 40 nm, vertical resolution 0.1 nm)
Contact angle measurement	Goniometer, developed in Laboratory for Thermal Technology (Faculty of Mechanical Engineering), using IDS UI-3060CP camera equipped with a microscope objective, and micrometer syringe Gilmont GS 1200 with a steel size 22 capillary tube (water droplet volume 10 μL)

Table 3
Topographical parameters, measured by optical interferometry. All data [with the exception of the reference surface (SS)] was filtered using a low-pass regression Gaussian filter.

Surface	Parameter			
	Sa(μm)	*Ssk*(/)	*Sku*(/)	*r* (/)
SS	0,07	−1,7	10,6	1,07
F1	0,65	−0,7	9,6	1,25
F2	0,71	−0,3	3,1	1,25
F3	0,78	0,4	3,4	2,02
F4 (1 st area)	1,36	−1,1	34,2	2,82
F4 (2nd area)	3,50	−1,3	7,4	5,87

uncertainty of the temperature and the heat flux measurements. The maximum expanded uncertainty of the heat transfer coefficient was determined to be 3.4 kW/m^{2}K.

3.3. Surface characterization

Laser textured surfaced were characterized using scanning electron microscopy (SEM), optical interferometry and through contact angle measurements. The equipment used is listed in Table 2. Using 3D optical microscope software analysis tools, we determined topographical parameters of the textured surfaces. The 3D space parameters *Sa*, *Ssk*, *Sku* and the roughness factor *r* were calculated. The wettability of the surfaces was measured through contact angles using a goniometer of our own design. Contact angles were recorded immediately after laser processing, after every boiling experiment, and irregularly over the course of 40 days after finishing the boiling experiments or after laser surface texturing.

4. Results and discussion

4.1. Surface microstructure

SEM images of the laser textured surfaces are shown in Fig. 5. Micro- and nanostructure depend heavily on the scan line separation and the laser pulse fluence. Despite low fluence, melting and ablation were achieved on surface F1 [e.g., see Fig. 5(a–c)]. The damage trail on the surface was narrower than the beam spot diameter on the surface and no splattering of the melted material was detected. Since the scan line separation was larger than the damage trail width, a "mesh" with untextured area appears after the laser processing. Additionally, the following interesting phenomenon can be observed in Fig. 5(b). The surface was firstly textured in the vertical direction and – in the second step – in the horizontal direction. In places where traces cross each other, it is clearly visible that the initial structure is fully erased by a second (horizontal) passage and (at these processing parameters) new structure depends on the direction of the second passage of the processing beam alone.

Surface F2 [e.g., see Fig. 5(d–f)] was textured using the same fluence as F1 but with a decreased scan line separation. Thusly, approximately 60% overlap between adjacent laser scanning lines was achieved. As it is clearly visible from Fig. 5(d–f), in this manner the whole area was structured. The microstructure on surface F2 is finer compared to the one on surface F1 with noticeable smaller droplets of melted material. However, some details are quite similar as it is visible from a comparison between Fig. 5(c) and (f).

For texturing of the surface F3 [e.g., see Fig. 5(g–i)], the same scan line separation was used as for the surface F2, but the laser pulse fluence was increased. As it is discernible from SEM micrographs, surface F3 included both micro- and nanostructure. However, exact identification of the latter proved impossible due to the limitation of the SEM image magnification and resolution. By increasing the fluence, some details were lost [e.g., comparison of Fig. 5(f) and (h)].

In contrast with homogenously processed surfaces F1–F3, surface F4 was textured with a variable scan line separation resulting in a non-uniform microstructure. Laser pulse fluence was increased in comparison with the surface F3 and periodically varied scan line separation from 10 μm to 200 μm by a step of 10 μm and then back from 200 μm to 10 μm was utilized. The SEM micrographs of the selected F4 area (the region with the smallest scan line separation in the vertical direction) are shown in Fig. 5(j–l). It is evident that surface F4 also appears to be slightly porous, while the increased pulse fluence resulted in the deepest and widest damage trails with clearly noticeable abundant melted material splashing. The adjacent laser scanning lines overlapped only in certain areas, i.e., where scan line separation was small enough. In these regions, various microcavities with the diameter of up to a few micrometers were detected along with microporosity, as marked on the right-hand side of Fig. 6, where the diameters of microcavities are also listed. From Fig. 6 it is clearly noticable that multi-scale microcavities appear in the region with the smallest scan line separation (10 μm). These cavities could potentially act as active nucleation sites in accordance with the aforementioned nucleation criteria. Furthermore, their diameter is not uniform and spans across at least one order of magnitude and it is therefore expedient for heat transfer enhancement.

The topographical parameters measured by optical interferometry are listed in Table 3. Here, all the results with the exception of the reference surface (SS) were filtered using a low-pass regression Gaussian filter. These results show that the highest roughness was achieved on surface F4, mainly due to the deepest damage trails of laser processing (as a result of the highest laser pulse fluence). In the case of surface F4, which had a non-uniform microstructure, measurements are listed for two selected areas. The data for the "1 st area" was obtained by measurements in the area processed by the highest scanning line separation (200 μm), while the data for the "2nd area" was measured in the area with the smallest scanning line separation (10 μm). Ratio between real surface area and the projected area, expressed by roughness factor *r*, could be upwards of five in certain regions of the surface F4.

4.2. Surface wettability

The measurements of the surface wettability were performed on *textured-only* surfaces and on textured surfaces (using the same laser parameters and, therefore, marked with the same labels) that were used in boiling experiments. Contact angle of a water droplet on a reference, untextured surface is shown on Fig. 7(a) and was equal to 88°. Immediately after the processing, surfaces F1 and F2 were slightly hydrophilic [e.g. see Fig. 7(b–c)], surface F3 was superhydrophilic [e.g. see Fig. 7(d)], while surface F4 exhibited non-uniform wettability due to the heterogeneous microstructure.

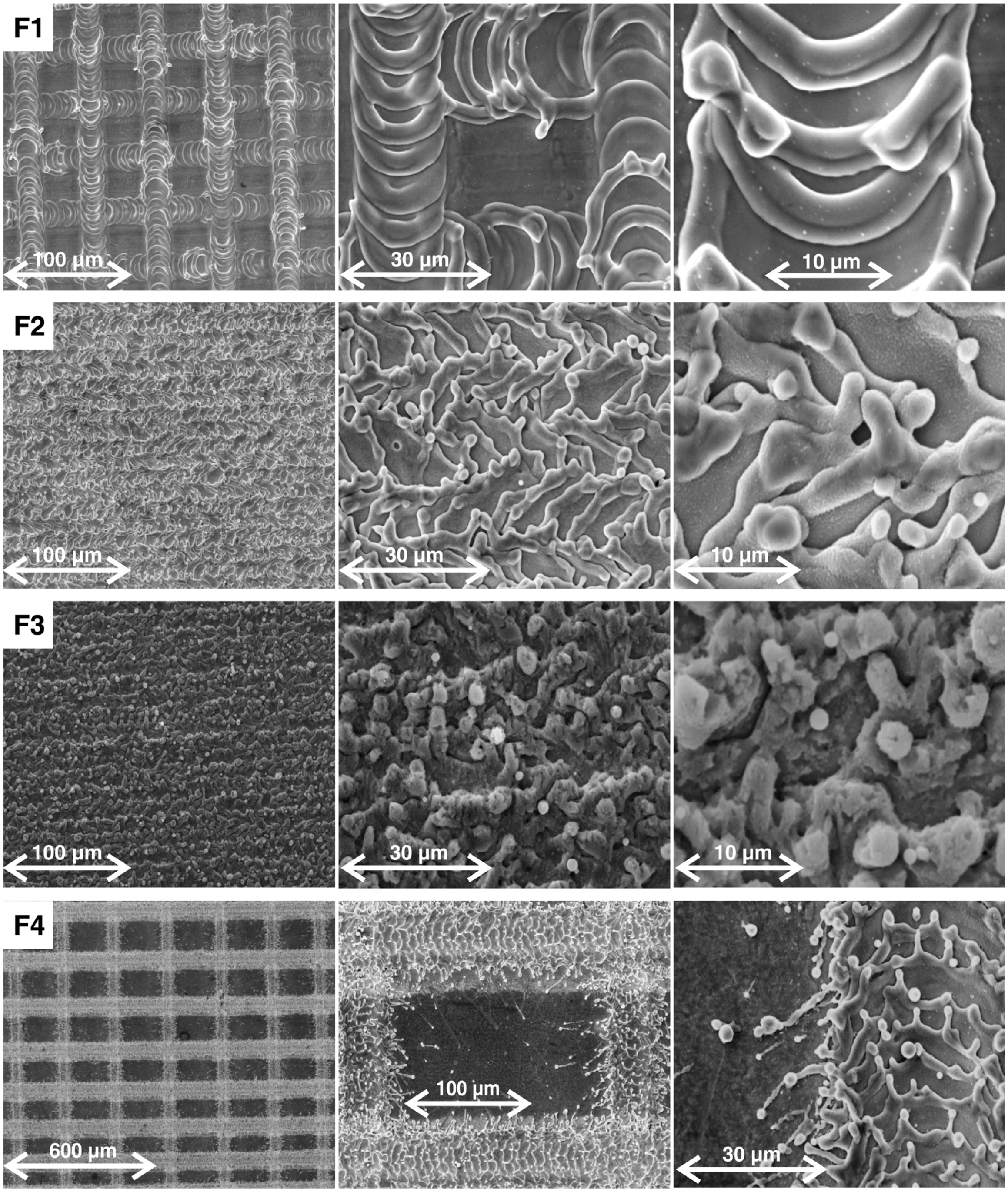

Fig. 5. SEM micrographs of the laser textured surfaces.

We also measured the temporal wettability development with the samples being exposed to the ambient air at room conditions. The results are shown in Fig. 7(e). Here, mark "b" in the legend corresponds to the surfaces that were used in boiling experiments after the processing. As it is visible from the presented results, the wettability of all of the surfaces decreased over time, similar to the observations of other authors [18,19,30]. Authors in Ref. [18] detected and increased amount of carbon on the stainless steel surface after being treated with femtosecond laser. However, the initial carbon amount is not enough to fully cover the structure and entire surface is superhydrophilic due to combination of underlying polar iron oxides and increased surface roughness. Over time, the decomposition of carbon dioxide into carbon takes place and starts to accumulate on the surface. In combination with dual-scale roughness structure this results in superhydrophobic surface. In their case, the superhydrophobicity was developed in about 10–30 days after the laser treatment. In our case, the contact angle increased by 20–40° depending on the surface-texturing parameters and it stabilized after approximately 15–20 days after the processing. No significant difference is observed between *textured-only* surfaces and surfaces used in boiling experiments. This result proves that the nanosecond laser texturing has a great potential in applications for improved boiling heat transfer, since it can ensure durability of the produced surfaces.

Sample F4, which was processed by a variable laser scan line separation, exhibits heterogeneous surface texture and therefore

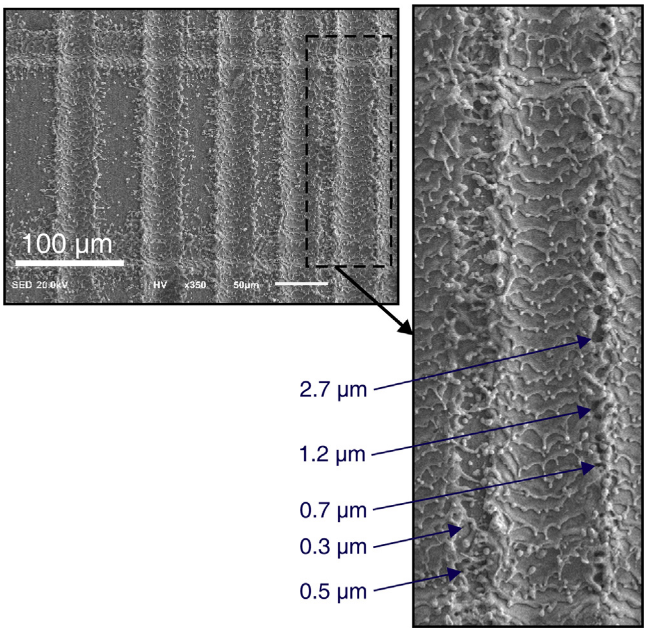

Fig. 6. SEM micrograph of the surface F4 in the region with the smallest scan line separation (10 µm); some microcavities are marked with arrows with their diameters also listed.

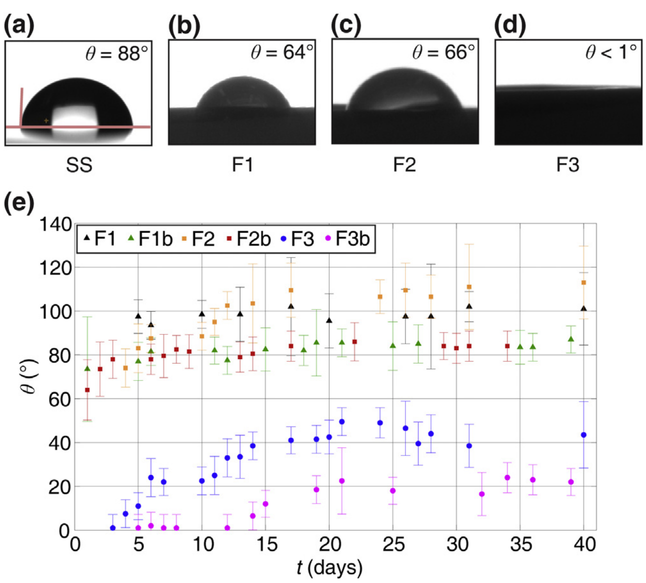

Fig. 7. (a–d) Wettability of bare stainless steel foil (SS) and surfaces F1–F3 immediately after the processing. (e) Temporal development of wettability for boiled (marked with 'b') and *textured-only* surfaces. Number of repeated trials for each measurement was 10. Error bars are showing.

also non-uniform wettability. We have measured the contact angles to be in between 66° and 142°.

4.3. Pool boiling performance

The pool boiling performance was firstly estimated by measuring the heat flux vs. surface overheat and heat transfer coefficient as a function of the heat flux, as shown in Fig. 8. We need to note that reference surface SS and laser-textured surface F1 were not able to dissipate higher heat fluxes than 300 kW/m^2 without the onset of the CHF conditions and data is therefore shown only for the measurable range for these surfaces. CHF obtained on thin substrates is not comparable with the CHF calculated from Zuber's theoretical model [31], which considers only hydrodynamic effects while ignoring heat transfer at the heated surface, thermal properties, and thickness of the surface. According to the existing correlations for thin heaters [32,33] the CHF for saturated water pool boiling on 25-µm stainless-steel foil is in the range from 0.2–0.6 of the asymptotic hydrodynamic CHF due to heater conductance/capacitance effect. For all other surfaces rather than SS and F1, we show boiling curves up to about 400 kW/m^2 and this heat flux does not represent the CHF.

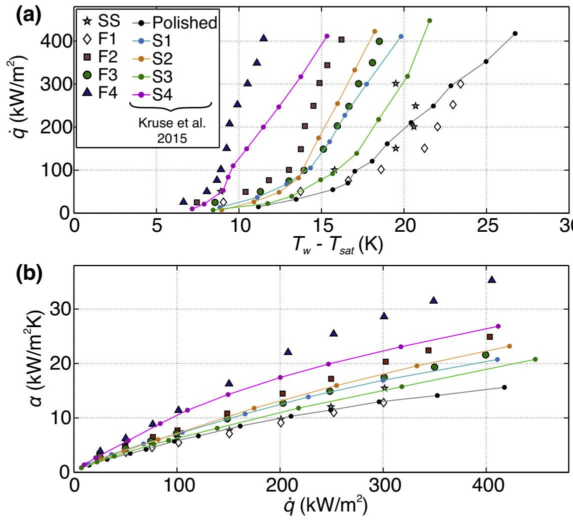

Fig. 8. (a) Heat flux as a function of superheat. (b) Heat transfer coefficient versus heat flux. The results are shown for our, nanosecond-laser textured, surfaces F1–F4 (unprocessed surface is denoted as SS). The dots connected by lines (S1–S4 and Polished) represent the results reported by Kruse et al. [5] and are shown for comparison.

For a comparison we also show on Fig. 8 the results obtained by Kruse et al. [5]. In their study, a femtosecond laser was used to produce superhydrophilic surfaces with self-organized, quasi-periodic microstructures covered by a layer of nanoparticles; 4 different surfaces (S1–S4) were created using different laser pulse fluences. Peak to valley height of the so produced microstructures ranged from 7.1 µm to 35.8 µm with the surface area ratio being in the range from 3.85 to 4.7 for the S1 and S4 samples, respectively. Their results for non-processed, polished surface are also shown in Fig. 8.

Secondly, we manually analyzed transient temperature fields of the boiling surface in order to determine the bubble nucleation frequency (f_b) and the active nucleation site density (N_d) at three different heat fluxes with the results presented in Fig. 9. The nucleation frequencies express the rate at which bubbles form and depart per a unit of time and active nucleation site density is the number of active nucleation sites divided by a unit area of heater surface. In boiling systems, it is desirable to have high active nucleation site densities and high nucleation frequencies in order to prevent the formation of large vapor covered areas and thus to prevent the formation of local dry-outs that could indicate the beginning of a boiling crisis [28,27]. Universally, it is noticeable that the frequencies and nucleation site densities increase with an increase of the heat flux, which coincides with the finding of other authors [23,34,35].

The results in Fig. 8(a) indicate that surface F1 provides no improvement over the reference surface, denoted with SS. The main reason for this probably lies in a too low laser pulse fluence resulting in very shallow modification of the treated surface. SEM analysis confirmed that F1 sample did not include any microcavities that could act as active nucleation sites, thus the nucleation frequency and nucleation site density are similar to the SS sample (e.g. see Fig. 9). In fact, the average wall superheat on surface F1

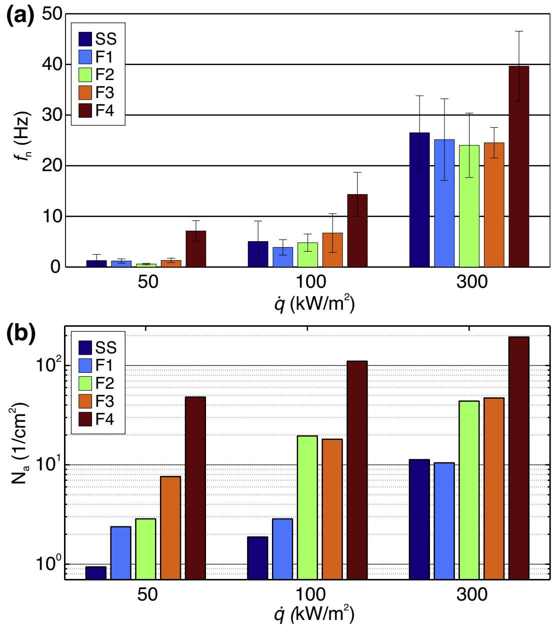

Fig. 9. Comparison of (a) nucleation frequencies and (b) active nucleation site densities at three different heat fluxes. Error bars in (a) indicate standard deviation.

is higher than for SS sample throughout entire experimental range (0–300 kW/m^2). This might be contributed to higher wettability of F1 (e.g. see Fig. 7) and the fact that higher wettability require more energy for the boiling incipience [36], which results in higher activation temperatures as well as higher average temperatures throughout the nucleate boiling regime. One should still be aware that differences between SS and F1 are within the measurement uncertainty.

Surfaces F2 and F3 with more significant, but still uniform microstructure and wettability, enable enhanced boiling heat transfer in regard to the reference surface. In the 0–300 kW/m^2 heat flux span, both surfaces provided an approximate 40% enhancement of the heat transfer coefficient compared to the SS sample. Even though the surface structure of F2 and F3 samples is similar, the average wall superheat for F3 was more than 1 K higher compared to F2 [see Fig. 8(a)]. Despite the fact that the expanded measurement uncertainty of IR camera is 2 K, the difference in average temperatures can be again contributed to the superhydrophilic nature of the F3 sample and therefore higher required energy for boiling incipience compared to F2.

The highest heat transfer enhancement was achieved on surface F4. In this case, we obtained higher heat fluxes at lower wall superheats, not only in comparison with the reference surface, but also in comparison with the state-of-the-art results presented by Kruse et al. [5]. Heat transfer coefficient on the surface F4 was more than two-times higher that on the SS sample [e.g. 110% enhancement, as visible from Fig. 8(b)], while nucleation frequency was also enhanced by a factor of two [see Fig. 9(a)] and nucleation site density was higher by more than one order of magnitude [see Fig. 9(b)].

4.4. Control of active nucleation sites by laser texturing

The control of active nucleation sites is one of the most challenging issues in boiling heat transfer. Therefore, it is extremely important to correlate the locations of active nucleation sites with the laser textured microstructure. In order to identify the locations of active nucleation sites, we performed appropriate image processing and analysis of the high-speed thermography recordings for all tested surfaces F1–F4 at the three different heat flux rates: 50 kW/m^2, 100 kW/m^2 and 300 kW/m^2. The results are presented in Fig. 10.

During each individual bubble growth the surface is rapidly cooled down due to the large local heat flux in the moment of vaporization. This round-shaped cold spot can be easily identified and measured with pixel resolution for each time frame based in IR thermographs. Therefore, we decided to add each detected nucleation area to some cumulative matrix. This matrix was then plotted as a grayscale image, as shown in each odd line in Fig. 10. Each circular shape on this grayscale image represents maximum bubble contact diameter, while the number of circles divided by the heater area corresponds to the active nucleation site density. To better display the spatial distribution of nucleation sites, we determined the center of each detected nucleation. The results are represented as the blue dots on a gray background in each even line of Fig. 10. To obtain these results, we analyzed 10 s of a recording (e.g. 10,000 frames) for each sample at each individual heat flux.

As it is discernable from the first row in Fig. 10, bubble contact diameters are the largest on surface F1 and range from 1.3 mm to 6.3 mm at 300 kW/m^2. Similarly to the unstructured stainless steel foil [27], F1 sample with shallow microstructure required high activation temperature, which resulted in large bubble contact diameters and a low nucleation frequency. Large bubbles also limit the total number of active nucleation sites. On surfaces F2 and F3 (e.g., see 3rd and 5th line in Fig. 10), bubble contact diameters are about two-times smaller compared to F1. Pronounced microstructure on F2 and F3 enhances potential active nucleation sites. Even though the contact angles on F1 and F2 are very comparable, we must emphasize that pronounced microstructure on F2 results in better wickability, which enhances heat transfer performance [37]. This confirms that contact angle itself (as a surface-fluid property) is not sufficient parameter to predict boiling behavior. Despite the nucleation site density enhancement on F2 and F3, the nucleations are still randomly distributed across the entire heater area, as it is clearly distinguishable from the spatial distributions of the active nucleation sites in Fig. 10.

The smallest bubbles were observed on surface F4 where the contact diameters at 300 kW/m^2 ranged from only 0.4 mm to 1.8 mm. An even more important result is presented in the last row of Fig. 10, where it is clearly visible that the active nucleation site density on surface F4 is periodically distributed across the entire surface and exactly matches the spatial distribution of the F4 areas with the smallest scan line separations. These areas are covered with multi-scale sized microcavities, as shown through surface analysis presented in Fig. 6. This is in agreement with the nucleation criteria (presented in Fig. 1) implying that in order to maximize the number of possible active nucleation sites the surface should provide micrometer and sub-micrometer sized cavities and also variable wettability. In addition to increasing active nucleation sites, the presence of micro cavities also lowered the onset of nucleate boiling for more than 5 K compared to bare stainless steel (e.g. see Fig. 8).

Although the resolution of IR thermography is limited and, consequently, the position of active nucleation sites should be more accurately determined by other state-of-the-art temperature mapping techniques in the future [38], our results prove that the number of nucleation sites was significantly higher in the vicinity of microcavities in comparison with other areas. These results, obtained on surface F4, confirm the predictions of the nucleation criteria and lead to an important conclusion that straightforward and cost-effective nanosecond laser texturing is able to produce cavities of diameters up to a few micrometers and surfaces with non-uniform wettability. This opens up an important possibility for controlling the boiling process in terms of defining active nucle-

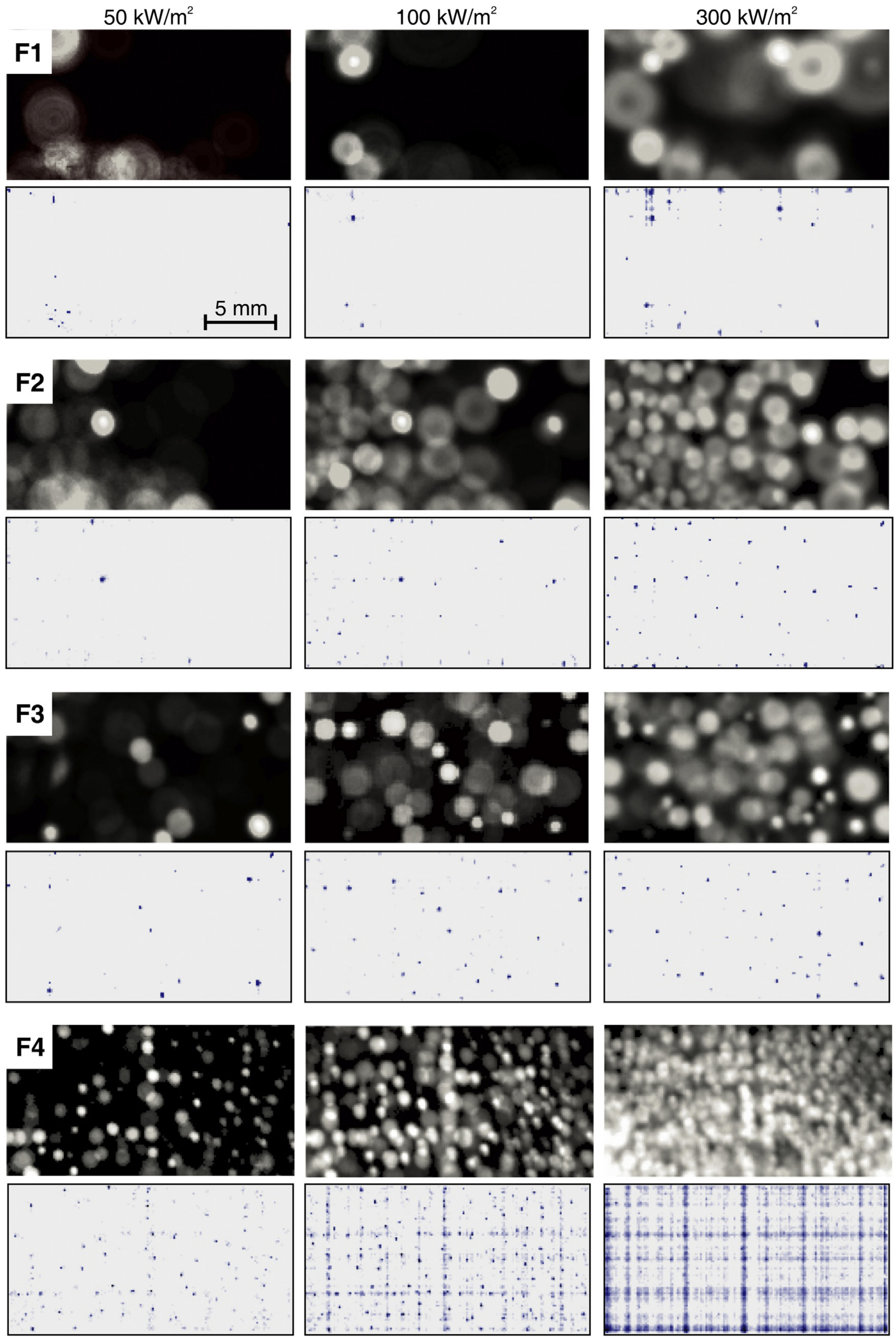

Fig. 10. Spatial distribution of active nucleation sites.

ation areas, bubble diameters and nucleation frequencies as well as density of active nucleation sites and finally wall superheat.

5. Conclusions

In this study we examined the potential of laser textured surfaces for enhanced boiling heat transfer. Multiple surfaces were prepared on thin stainless steel foils by using different laser texturing patterns and different laser pulse fluences. Prepared samples were either hydrophilic, superhydrophilic or had non-uniform wettability depending on the combination of the processing parameters. The wettability decreased over time and stabilized in approximately two to three weeks. The comparison between *textured-only* surfaces and surfaces used in boiling proved the stability of laser-textured surfaces in boiling experiments.

Nucleate boiling heat transfer on textured surfaces was evaluated by means of high-speed IR thermography. The obtained results lead to the following important conclusions:

- Laser textured surfaces are able to enhance nucleate boiling heat transfer with lower superheats and up to 110% higher heat transfer coefficients compared to the untextured surface.
- Under certain texturing parameters, non-uniformly wettable surface structure with multi-scale microcavities is formed through melting and setting of the material. Our results show that these features are responsible for achieving 20–40 times higher active nucleation site density compared to the bare untreated surface. IR thermographs proved that most nucleations happened in the vicinity of the microcavities. This is also in agreement with the described theoretical nucleation criteria.
- Through the control of texturing parameters, the location of microcavities can be controlled and consequently also the areas where the majority of the bubbles form and grow. This suggests that laser texturing technique enables some control over the complex boiling process.

The presented surface modification technique does not require any additional coatings and/or post-processing. Results prove that marking nanosecond laser allows modification of surfaces for an increased boiling heat transfer performance. This is an important demonstration, since cheaper production (in comparison with micro- and nanostructuring through the use of ultrafast, i.e., ps and fs laser systems) enables wider dissemination of surfaces with enhanced functionalities in different areas of applications.

Acknowledgement

The authors acknowledge the financial support from the state budget by the Slovenian Research Agency (Programme Nos. P2-0223 and P2-0392).

References

[1] C.H. Wang, V.K. Dhir, Effect of surface wettability on active nucleation site density during pool boiling of water on a vertical surface, J. Heat Transf. 115 (1993) 659–669, http://dx.doi.org/10.1115/1.2910737.

[2] B. Bourdon, P. Di Marco, R. Rioboo, M. Marengo, J. De Coninck, Enhancing the onset of pool boiling by wettability modification on nanometrically smooth surfaces, Int. Commun. Heat Mass Transf. 45 (2013) 11–15, http://dx.doi.org/10.1016/j.icheatmasstransfer.2013.04.009.

[3] M. Zupančič, M. Steinbücher, P. Gregorčič, I. Golobič, Enhanced pool-boiling heat transfer on laser-made hydrophobic/superhydrophilic polydimethylsiloxane-silica patterned surfaces, Appl. Therm. Eng. 91 (2015) 288–297, http://dx.doi.org/10.1016/j.applthermaleng.2015.08.026.

[4] H.S. Ahn, H.J. Jo, S.H. Kang, M.H. Kim, Effect of liquid spreading due to nano/microstructures on the critical heat flux during pool boiling, Appl. Phys. Lett. 98 (2011) 98–101, http://dx.doi.org/10.1063/1.3555430.

[5] C.M. Kruse, T. Anderson, C. Wilson, C. Zuhlke, D. Alexander, G. Gogos, S. Ndao, Enhanced pool-boiling heat transfer and critical heat flux on femtosecond laser processed stainless steel surfaces, Int. J. Heat Mass Transf. 82 (2015) 109–116, http://dx.doi.org/10.1016/j.ijheatmasstransfer.2014.11.023.

[6] A.R. Betz, J. Jenkins, C.J. Kim, D. Attinger, Boiling heat transfer on superhydrophilic, superhydrophobic, and superbiphilic surfaces, Int. J. Heat Mass Transf. 57 (2013) 733–741, http://dx.doi.org/10.1016/j.ijheatmasstransfer.2012.10.080.

[7] I. Golobič, M. Zupančič, Wall-temperature distributions of nucleate pool boiling surfaces vs boiling curves: a new approach, Int. J. Heat Mass Transf. 99 (2016) 541–547, http://dx.doi.org/10.1016/j.ijheatmasstransfer.2016.04.033.

[8] S.K. C.S, S. S, A. C.R, S.K. M.C, P. A.S, R. K, Flow boiling heat transfer enhancement on copper surface using Fe doped Al2O3–TiO2 composite coatings, Appl. Surf. Sci. 334 (2015) 102–109, http://dx.doi.org/10.1016/j.apsusc.2014.08.076.

[9] C.-H. Choi, M. David, Z. Gao, A. Chang, M. Allen, H. Wang, C. Chang, Large-scale generation of patterned bubble arrays on printed Bi-functional boiling surfaces, Sci. Rep. 6 (2016) 23760, http://dx.doi.org/10.1038/srep23760.

[10] C.Y. Lee, B.J. Zhang, K.J. Kim, Morphological change of plain and nano-porous surfaces during boiling and its effect on nucleate pool boiling heat transfer, Exp. Therm. Fluid Sci. 40 (2012) 150–158, http://dx.doi.org/10.1016/j.expthermflusci.2012.02.011.

[11] S. Vemuri, K.J. Kim, Pool boiling of saturated FC-72 on nano-porous surface, Int. Commun. Heat Mass Transf. 32 (2005) 27–31, http://dx.doi.org/10.1016/j.icheatmasstransfer.2004.03.020.

[12] Y.Y. Hsu, On the size range of active nucleation cavities on a heating surface, J. Heat Transf. 84 (1962) 207–213.

[13] S.G. Kandlikar, V.R. Mizo, M.D. Cartwright, E. Ikenze, Bubble nucleation and growth characteristics in subcooled flow boiling of water, in: ASME Proc 32nd Natl. Heat Transf. Conf., ASME, 1997, pp. 11–18.

[14] S. Gong, P. Cheng, X. Quan, Two-dimensional mesoscale simulations of saturated pool boiling from rough surfaces. Part I: bubble nucleation in a single cavity at low superheats, Int. J. Heat Mass Transf. (2016), http://dx.doi.org/10.1016/j.ijheatmasstransfer.2016.04.085.

[15] D. Deng, R. Chen, Y. Tang, L. Lu, T. Zeng, W. Wan, A comparative study of flow boiling performance in reentrant copper microchannels and reentrant porous microchannels with multi-scale rough surface, Int. J. Multiph. Flow. 72 (2015) 275–287, http://dx.doi.org/10.1016/j.ijmultiphaseflow.2015.01.004.

[16] Y.-W. Lu, S.G. Kandlikar, Nanoscale surface modification techniques for pool boiling Enhancement. A critical review and future directions, Heat Transf. Eng. 32 (2011) 827–842, http://dx.doi.org/10.1080/01457632.2011.548267.

[17] A.Y. Vorobyev, C. Guo, Multifunctional surfaces produced by femtosecond laser pulses, J. Appl. Phys. 117 (2015) 33103, http://dx.doi.org/10.1063/1.4905616.

[18] A.M. Kietzig, S.G. Hatzikiriakos, P. Englezos, Patterned superhydrophobic metallic surfaces, Langmuir 25 (2009) 4821–4827, http://dx.doi.org/10.1021/la8037582.

[19] V.D. Ta, A. Dunn, T.J. Wasley, J. Li, R.W. Kay, J. Stringer, P.J. Smith, E. Esenturk, C. Connaughton, J.D. Shephard, Laser textured superhydrophobic surfaces and their applications for homogeneous spot deposition, Appl. Surf. Sci. 365 (2016) 153–159, http://dx.doi.org/10.1016/j.apsusc.2016.01.019.

[20] W.M. Rohsenow, A method of correlating heat transfer data for surface boiling of liquids, Trans. ASME 74 (1952) 969–976.

[21] S.G. Bankoff, Entrapment of gas in the spreading of a liquid over a rough surface, AIChE J. 4 (1958) 24–26, http://dx.doi.org/10.1002/aic.690040105.

[22] P. Griffith, J.D. Wallis, The role os surface conditions in nucleate boiling, Chem. Eng. Prog. Symp. 56 (1960) 49–63.

[23] C.-Y. Han, P. Griffith, The mechanism of heat transfer in nucleate pool boiling—part II, Int. J. Heat Mass Transf. 8 (1965) 905–914, http://dx.doi.org/10.1016/0017-9310(65)90074-8.

[24] H.S. Carslaw, J.C. Jaeger, Conduction of Heat in Solids, second ed., Oxford University Press, London, 1959.

[25] S.G. Kandlikar, Nucleation characteristics and stability considerations during flow boiling in microchannels, Exp. Therm. Fluid Sci. 30 (2006) 441–447, http://dx.doi.org/10.1016/j.expthermflusci.2005.10.001.

[26] H. Kim, J. Buongiorno, Detection of liquid-vapor-solid triple contact line in two-phase heat transfer phenomena using high-speed infrared thermometry, Int. J. Multiph. Flow 37 (2011) 166–172, http://dx.doi.org/10.1016/j.ijmultiphaseflow.2010.09.010.

[27] J. Petkovsek, Y. Heng, M. Zupancic, H. Gjerkes, F. Cimerman, I. Golobic, IR thermographic investigation of nucleate pool boiling at high heat flux, Int. J. Refrig. 61 (2016) 127–139, http://dx.doi.org/10.1016/j.ijrefrig.2015.10.018.

[28] T.G. Theofanous, T.N. Dinh, J.P. Tu, A.T. Dinh, The boiling crisis phenomenon part II: dryout dynamics and burnout, Exp. Therm. Fluid Sci. 26 (2002) 793–810, http://dx.doi.org/10.1016/S0894-1777(02)00193-0.

[29] J. Yoo, C.E. Estrada-Perez, Y.A. Hassan, An accurate wall temperature measurement using infrared thermometry with enhanced two-phase flow visualization in a convective boiling system, Int. J. Therm. Sci. 90 (2015) 248–266, http://dx.doi.org/10.1016/j.ijthermalsci.2014.12.007.

[30] D.V. Ta, A. Dunn, T.J. Wasley, R.W. Kay, J. Stringer, P.J. Smith, C. Connaughton, J.D. Shephard, Nanosecond laser textured superhydrophobic metallic surfaces and their chemical sensing applications, Appl. Surf. Sci. 357 (2015) 248–254, http://dx.doi.org/10.1016/j.apsusc.2015.09.027.

[31] N. Zuber, On the stability of boiling heat transfer, Trans. Am. Soc. Mech. Eng. 80 (1958) 711–720.

[32] I. Golobic, A.E. Bergles, Effects of heater-side factors on the saturated pool boiling critical heat flux, Exp. Therm. Fluid Sci. 15 (1997) 43–51, http://dx.doi.org/10.1016/S0894-1777(96)00170-7.

[33] M. Arik, A. Bar-Cohen, Effusivity-based correlation of surface property effects in pool boiling CHF of dielectric liquids, Int. J. Heat Mass Transf. 46 (2003) 3755–3764, http://dx.doi.org/10.1016/S0017-9310(03)00215-1.
[34] N. Zuber, Nucleate boiling. The region of isolated bubbles and the similarity with natural convection, Int. J. Heat Mass Transf. 6 (1963) 53–78, http://dx.doi.org/10.1016/0017-9310(63)90029-2.
[35] H.J. Ivey, Relationships between bubble frequency, departure diameter and rise velocity in nucleate boiling, Int. J. Heat Mass Transf. 10 (1967) 1023–1040, http://dx.doi.org/10.1016/0017-9310(67)90118-4.
[36] B. Bourdon, R. Rioboo, M. Marengo, E. Gosselin, J. De Coninck, Influence of the wettability on the boiling onset, Langmuir 28 (2012) 1618–1624, http://dx.doi.org/10.1021/la203636a.
[37] M.M. Rahman, E. Ölçeroğlu, M. McCarthy, Role of wickability on the critical heat flux of structured superhydrophilic surfaces, Langmuir 30 (2014) 11225–11234, http://dx.doi.org/10.1021/la5030923.
[38] I. Sedmak, I. Urbančič, R. Podlipec, J. Štrancar, M. Mortier, I. Golobič, Submicron thermal imaging of a nucleate boiling process using fluorescence microscopy, Energy 109 (2016) 436–445, http://dx.doi.org/10.1016/j.energy.2016.04.121.